Published by
NIGERIAN SOCIETY OF PHYSICAL SCIENCES
Available online @ https://journal.nsps.org.ng/index.php/jnsps

J. Nig. Soc. Phys. Sci. 9 (2027) 3905

Journal of the Nigerian Society of Physical Sciences

Structural controls and hydrothermal alteration prospectivity in part of the Ilesha schist belt, southwestern Nigeria: insights from integrated aeromagnetic and aeroradiometric data

Akindeji Opeyemi Fajana*, Israel Enaburekan Osemudiame, Morufu Tope Aroyehun

Department of Geophysics, Federal University Oye-Ekiti, Nigeria

Abstract

Hydrothermal mineral exploration in the Ife-Ilesha Schist Belt is complicated by poor rock exposure, intense weathering and the non-unique geophysical expression of lithology, structure and alteration. Although previous investigations have mapped regional structures and radiometric variations, the local spatial relationship between magnetic structural corridors and near-surface radioelement signatures remains insufficiently constrained in the investigated sector. This study integrates high-resolution aeromagnetic and airborne gamma-ray spectrometric data obtained from the Nigerian Geological Survey Agency to delineate geophysically prospective zones with possible hydrothermal mineralisation. Magnetic processing comprised reduction to the equator, regional-residual separation, first horizontal and vertical derivatives, second horizontal derivative, analytic-signal amplitude, tilt derivative, lineament interpretation and Euler deconvolution. Radiometric interpretation used potassium (K, %), equivalent uranium (eU, ppm), equivalent thorium (eTh, ppm), K/eTh ratio, F-parameter and ternary K-eTh-eU imagery. Across the mapped area, K ranges from approximately 0.2 to 2.4%, eTh from 5.4 to 23.8 ppm and eU from 0.6 to 4.9 ppm. The total magnetic intensity ranges from -208.3 to 149.7 nT, the reduced-to-equator field from -188.4 to 123.3 nT and the residual field from -96.5 to 75.6 nT. The strongest exploration significance occurs where structurally complex magnetic gradients and interpreted lineaments coincide spatially with elevated K/eTh and F-parameter responses, particularly in the northern and southeastern sectors. These coincidence responses are interpreted cautiously as priority zones for follow-up investigation because single-channel radioelement highs and magnetic anomalies are non-unique. The results refine the local structural-radiometric framework of the belt and identify testable exploration targets in the study area.

DOI: 10.46481/jnsps.2027.3905

Keywords: Aeromagnetic data, Aeroradiometric data, Mineral deposits, Hydrothermal mineralisation, Alteration zones

Article History:
Received: 25 August 2026
Received in revised form: 08 September 2026
Accepted for publication: 08 October 2026
Available online: 23 November 2026

© 2027 The Author(s). Published by the Nigerian Society of Physical Sciences under the terms of the Creative Commons Attribution 4.0 International license. Further distribution of this work must maintain attribution to the author(s) and the published article's title, journal citation, and DOI.

Communicated by: T. O. Ale

1. Introduction

Hydrothermal mineral systems are commonly controlled by lithology, intrusive activity, and permeable structures such as faults, joints, and shear zones [1–3]. Hydrothermal fluids can alter magnetic minerals and redistribute mobile radioelements, producing geophysical responses that are useful in exploration when interpreted within an appropriate geological framework [4, 5]. However, neither magnetic nor radiometric anomalies provide unique evidence of mineralisation. Magnetic responses may reflect lithology, structure, magnetite destruction or enrichment, and remanent magnetisation, while airborne gamma-ray spectrometry mainly records the near-surface distribution of K, eU, and eTh and may be influenced by weathering, soil devel-

*Corresponding Author Tel. No.: +234-803-825-9701.
Email address: akindeji.fajana@fuoye.edu.ng (Akindeji Opeyemi Fajana)

opment, moisture, vegetation, and surface water [5–7].

The Ife-Ilesha Schist Belt is a major mineralized basement terrain and contains quartz veins, metasedimentary and metavolcanic rocks, granitoids, amphibolites, and brittle-ductile structures associated with gold occurrences [8–13]. Previous investigations have shown the value of aeromagnetic, radiometric, remote-sensing, and prospectivity methods across the wider belt [12–18]. According to Ref. [16], aeromagnetic data were used to characterize structures favourable for mineralisation in the southern Ilesha Belt. Salawu *et al.* [17] integrated satellite, magnetic, and radiometric data and identified major NE-SW, NNE-SSW, and E-W structural trends together with radiometric contrasts along the Ifewara shear zone. Okeyode *et al.* [18] also documented the regional airborne magnetic and radiometric characteristics of Ilesha and its environs. Similar integrated studies outside the belt have shown that structural complexity, lineament density, and hydrothermal alteration indicators can support the delineation of mineral-potential zones [19], while high-resolution aeromagnetic and VLF-EM data have been used in typical crystalline basement terrain to identify structures associated with lead mineralisation and define targets for follow-up investigation [20].

Despite these advances, important uncertainties remain within the sector examined in this study. Regional investigations do not fully resolve the local spatial relationship between magnetic structural corridors and radiometric alteration proxies, and some earlier interpretations rely strongly on individual magnetic or radioelement anomalies even though such responses are non-unique. A more reliable approach therefore requires the convergence of independent structural and radiometric evidence rather than interpretation based on a single anomaly or colour class.

Airborne gamma-ray spectrometry is useful for mapping near-surface variations in K, eU, and eTh and for supporting lithological and alteration mapping [21]. Potassium may increase during potassic alteration, but high K may also reflect felsic lithology. Uranium is relatively mobile under many near-surface geochemical conditions, whereas Th is generally less mobile and commonly shows stronger lithologic control [5, 7, 22, 23]. For this reason, K/eTh and multichannel radioelement relationships are generally more informative than the absolute magnitude of a single radioelement. Aeromagnetic data complement these observations by imaging contrasts in magnetisation and their spatial gradients. In southwestern Nigeria, integrated aeromagnetic and gamma-ray spectrometric analysis at Ikogosi Warm Spring has been used to relate major structures and subsidiary faults to fluid pathways and exploration targets [24]. More broadly, the integration of geophysical datasets that respond to different physical properties and depth ranges can improve mineral-system interpretation [25]. Edge-enhancement methods such as the horizontal derivative, analytic-signal amplitude, and tilt derivative can delineate contacts and faults, while Euler deconvolution can provide source-location and depth estimates when the structural index and solution-quality criteria are clearly defined [26–31].

Accordingly, this study integrates magnetic derivatives and interpreted lineaments with joint K-eU-eTh behaviour, K/eTh, and F-parameter responses in a focused part of the Ife-Ilesha Schist Belt. The specific objectives are to delineate magnetic gradients, contacts, and lineaments that may represent structurally permeable corridors; characterize near-surface radioelement variations without treating isolated single-channel anomalies as definitive evidence of alteration; identify priority prospective zones where independent magnetic and radiometric criteria spatially coincide; and compare the resulting structural and radiometric patterns with previously published observations from the Ife-Ilesha Schist Belt.

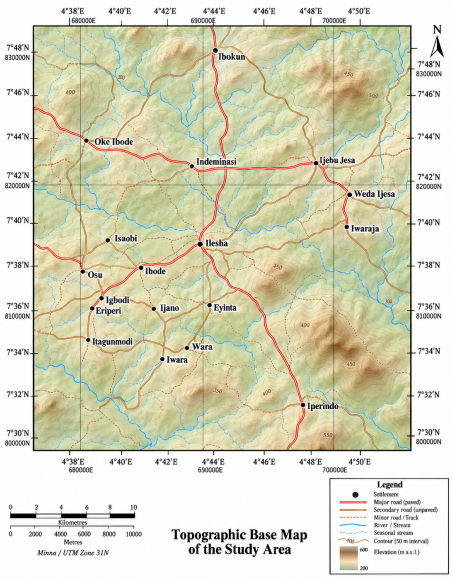

Figure 1: Topographic base map of the study area.

The study therefore provides a concise, locally focused structural-radiometric interpretation and a transparent framework for selecting zones that warrant follow-up mineral exploration. This staged approach is consistent with established mineral-exploration practice, in which reconnaissance evidence is integrated before progressively more detailed evaluation [32].

2. The study area

The study area lies within the Ilesha Schist Belt in the southwestern part of Nigeria (Figure 1), and it covers several towns such as Ilesha, Ibodi, Iloko-Ijesha, Idominasi, Iyemogun, Iwara, Eyinta, Isaobi, Ijano, Osu, Eriperi, Igunmo, and Wara. The Ilesha Schist Belt lies within the Precambrian Basement Complex of Nigeria, and it is known for gold mineralisation and other mineral resources associated with hydrothermal processes [8, 15] in the study area. The area lies between Latitude 7° 49I 50.08II N and 7° 79I 48.49II N and Longitude 4° 59I 70.12II E and 4° 83I 60.23II E, corresponding to UTM Eastings 828791–829605 m and Northings 676221–676448 m (WGS 84, UTM Zone 31N).

The study area is easily accessible through the Ilesha-Akure expressway and numerous extensive secondary roads that connect Ilesha with neighbouring communities such as Ibodi, Idominasi, Iloko-Ijesha, and Iwara. The study area is

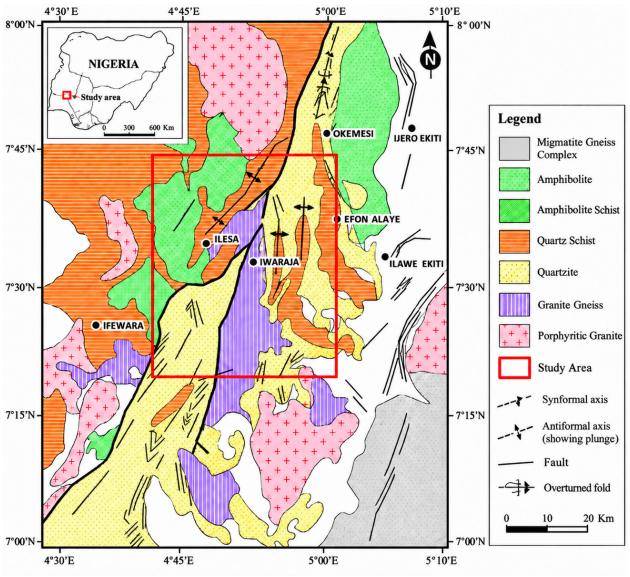

Figure 2: Geological map of Ilesha Schist Belt showing the study area. Adapted from Ref. [15].

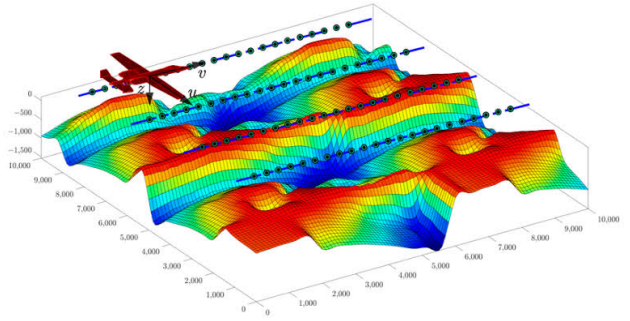

Figure 3: Simulation diagram of aeromagnetic survey flight. After Ref. [46].

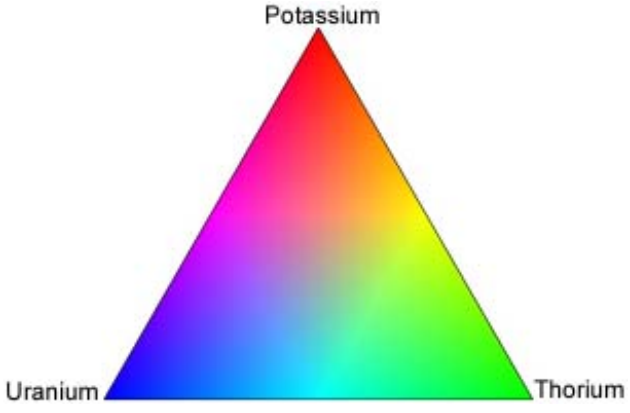

Figure 4: Maxwell colour triangle. After Ref. [47].

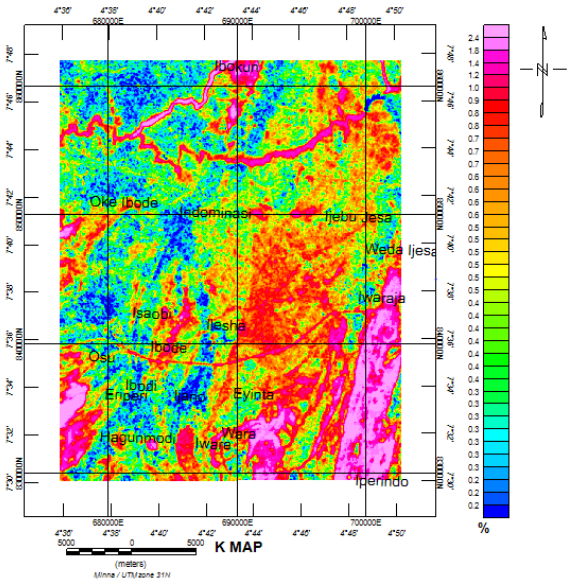

Figure 5: Potassium (K) concentration map showing distinct high- and low-K domains reflecting spatial variations in surface lithology.

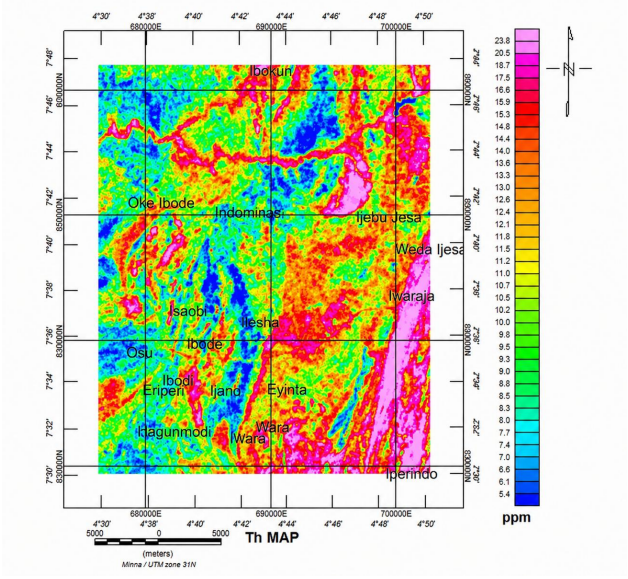

Figure 6: Thorium (eTh) concentration map showing contrasting zones of relative enrichment and depletion across the study area.

characterized by undulating to moderately rugged terrain typical of the Ilesha Schist Belt. The relief consists of gently sloping plains that are separated by ridges, isolated hills, and rocky outcrops that are relatively resistant to weathering. The topography reflects prolonged weathering and erosion of the Precambrian Basement Complex rocks in the area [33, 34]. The study area lies within the rainforest-derived savannah transition zone of southwestern Nigeria. Human activities have produced secondary forests dominated by farmlands, shrubs, and grasses. The common economic crops in the area include maize, cassava, cocoa, plantain, and yam [8, 35]. The drainage pattern is mainly dendritic, a characteristic of crystalline basement terrains. The rivers and streams contribute to the erosion, weathering, and sediment transportation of the crystalline rocks found in the area [9, 34, 36].

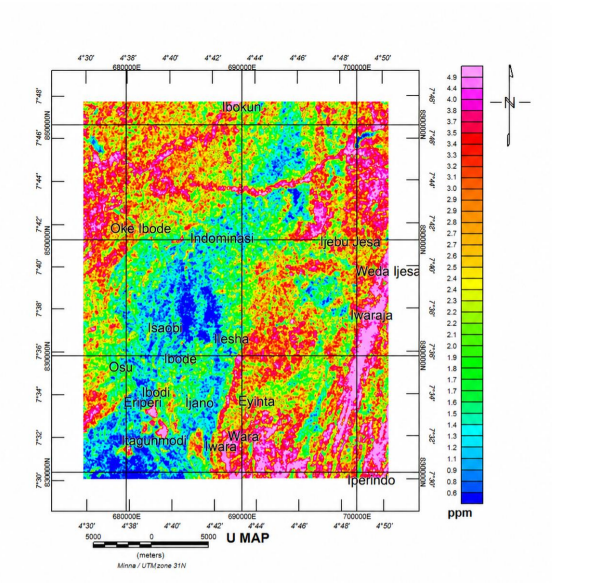

Figure 7: Uranium (eU) concentration map showing marked spatial variations in radioelement distribution.

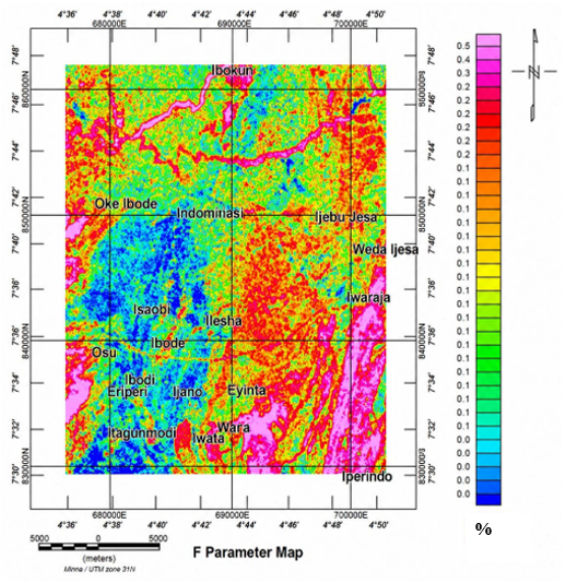

Figure 9: F-parameter map showing localized zones of relatively elevated radiometric response.

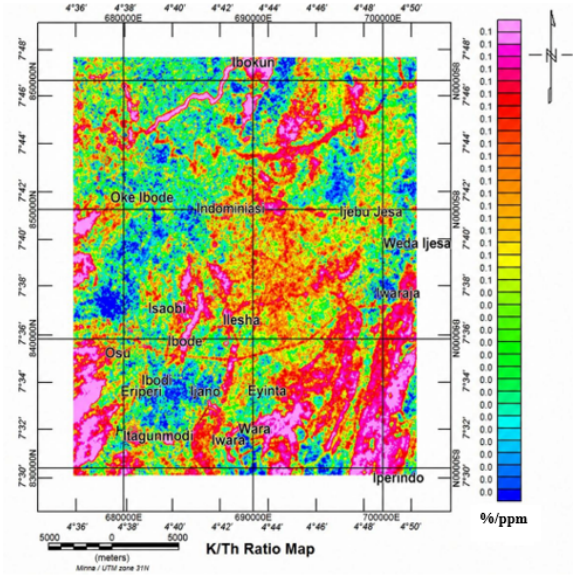

Figure 8: K/Th ratio map highlighting contrasting low- and high-ratio radiometric domains.

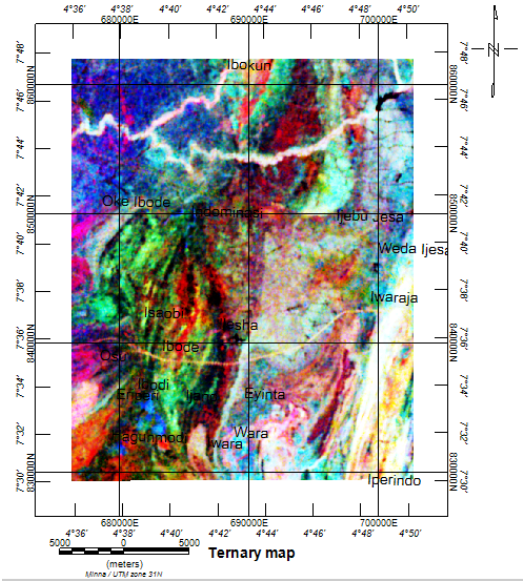

Figure 10: Ternary K-eTh-eU map showing spatial variations in the relative contributions of the three radioelements.

2.1. Geologic setting of the study area

The study area is characterized by monocyclic Proterozoic metasedimentary and metavolcanic rock units deposited on the polycyclic Archaean basement complex [10] (Figure 2). It consists of quartzite, quartz schist, amphibolite, mica schist, and banded iron formation that is intruded by granite, veins, and pegmatites. The hydrothermal mineralisation in the area is structurally controlled by the Ifewara Fault Zone [9, 11]. The rocks found in the area have undergone deformation, resulting in faults, folds, joints, and shear zones [9, 33, 37]. The quartz veins found in the area host hydrothermal mineralisation [12, 13]

3. Materials and methods

The aeromagnetic and airborne gamma-ray spectrometric datasets used in this study were obtained from the Nigerian Geological Survey Agency (NGSA) for Ilesha Sheet 243 and form part of the national high-resolution airborne geophysical survey undertaken by Fugro Airborne Surveys. Published metadata for Sheet 243 indicate that acquisition extended from 7 December 2006 to 31 May 2007, with subsequent processing by Fugro. The magnetic survey employed three Scintrex CS-3/C53 caesium-vapour magnetometers mounted on fixed-wing aircraft, with measurements recorded at approximately 0.1 s in-

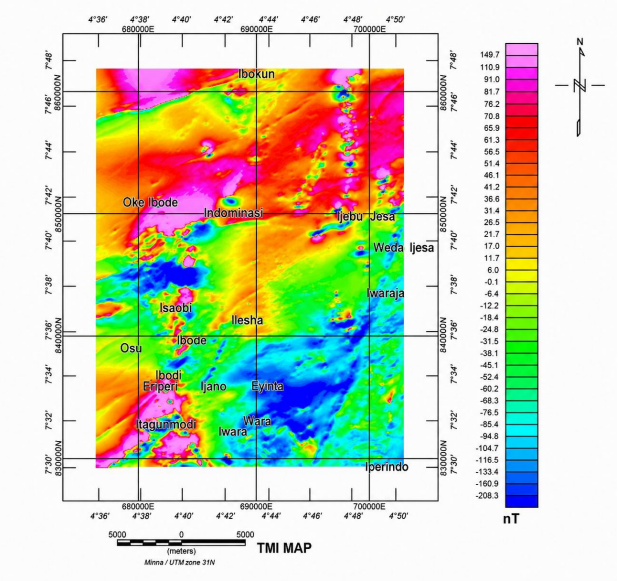

Figure 11: Total magnetic intensity (TMI) map.

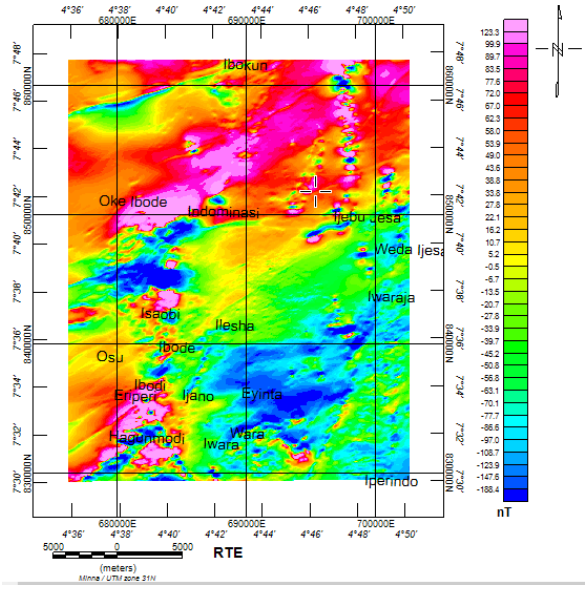

Figure 12: Reduced-to-equator magnetic map showing amplitudes of −188.4 to 123.3 nT and prominent magnetic gradients and anomaly boundaries.

tervals, equivalent to about 7 m along the flight path. Flight lines were spaced at 500 m, oriented NW-SE at approximately 135°, and flown at a mean terrain clearance of about 80 m, with NE-SW tie lines at approximately 45°. The corresponding radiometric data were recorded at approximately 1 s intervals, about 75 m, using a 512-channel gamma-ray spectrometer equipped with NaI(Tl) scintillation detectors.

Standard contractor preprocessing of the magnetic data included diurnal correction, levelling and micro-levelling, removal of cultural and spurious responses, magnetic compensation and removal of the International Geomagnetic Reference Field. The International Geomagnetic Reference Field (IGRF)

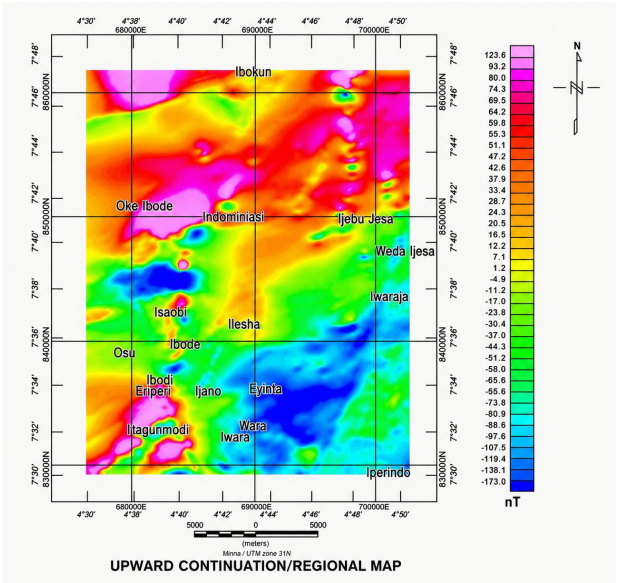

Figure 13: Upward-continued magnetic map at 500 m, emphasizing broad regional magnetic trends while suppressing shallow anomalies.

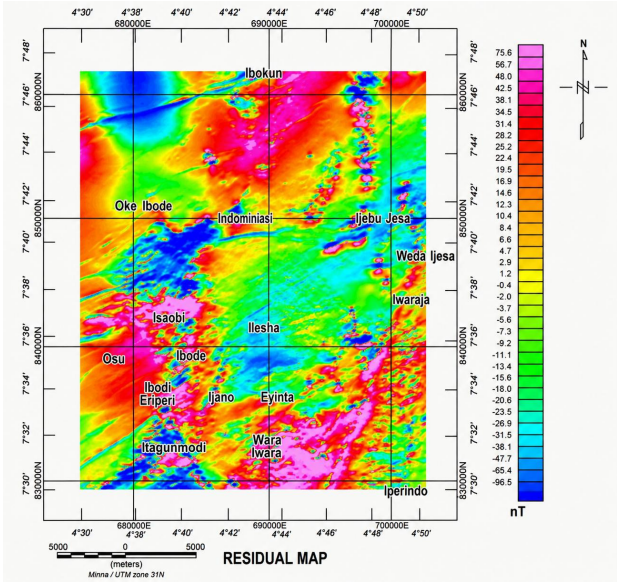

Figure 14: Residual magnetic map showing values of −96.5 to 75.6 nT and short-wavelength anomalies associated with shallow magnetic sources.

2005 model was applied to the aeromagnetic dataset. The reference epoch was 31 May 2007, with a magnetic inclination of −10.717° and declination of −1.853°. These field parameters were subsequently used for the reduction-to-the-equator (RTE) transformation. The magnetic data were subsequently interpolated by minimum-curvature gridding for map production. All subsequent processing and map production were carried out in Oasis Montaj using WGS 84/UTM Zone 31N (Figure 3).

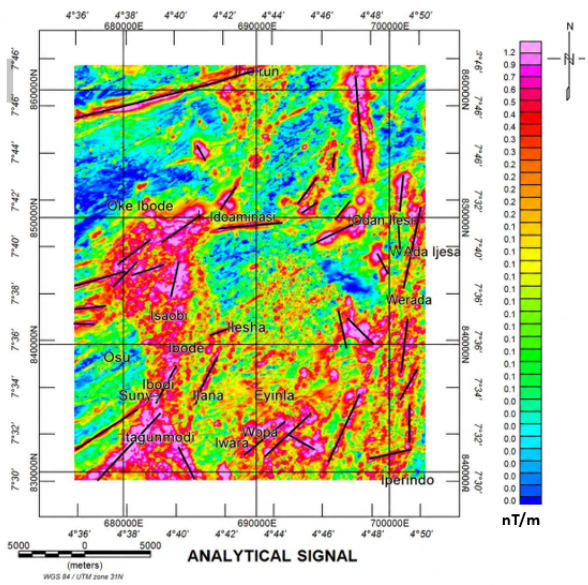

Figure 15: Analytic signal amplitude map highlighting major magnetic-source boundaries and zones of enhanced magnetic gradients.

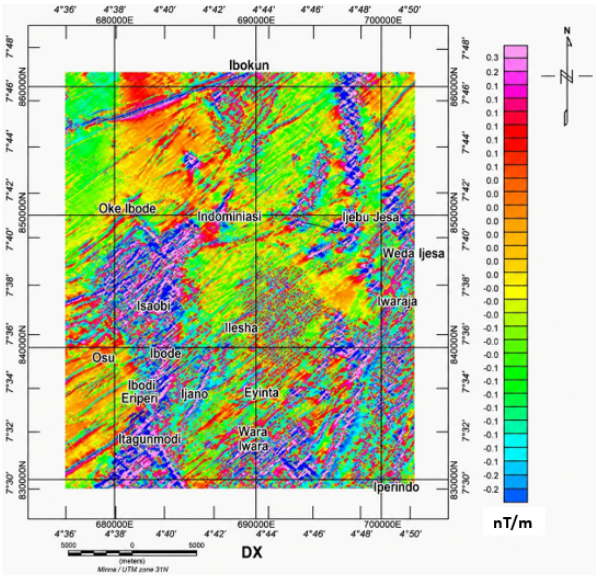

Figure 17: First-order derivative in the X-direction (Dx) map.

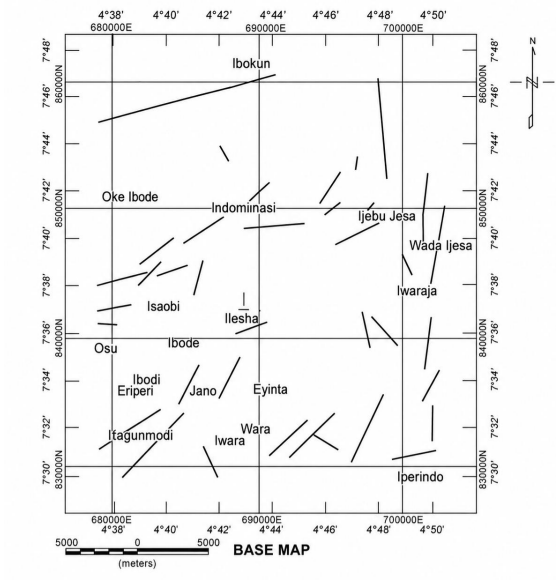

Figure 16: Lineaments interpreted from the analytic signal map.

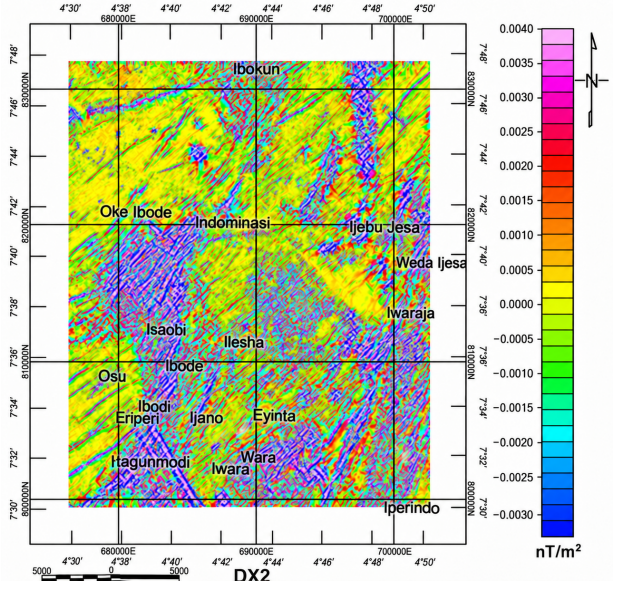

Figure 18: Second-order derivative in the X-direction (Dxx) map.

3.1. Airborne gamma-ray spectrometric data processing

Airborne gamma-ray spectrometry measures gamma radiation emitted by naturally occurring K, U-series and Th-series radionuclides in the uppermost part of the ground surface. Because gamma rays are strongly attenuated, the response is dominated by near-surface material rather than deep subsurface rocks [5, 22, 23]. Potassium is reported as K (%), whereas uranium and thorium are reported as equivalent concentrations, eU (ppm) and eTh (ppm), on the assumption of secular equilibrium within their decay series. Disequilibrium, weathering, leaching, soil moisture, vegetation and surface water can modify the measured response. Accordingly, the K, eU and eTh maps were interpreted jointly. The K/eTh ratio and F-parameter were used as alteration-sensitive indices, while the ternary composite was interpreted first as relative K-eTh-eU abundance and only subsequently in geological context. Comparable aeroradiometric work in the Nigerian Basement Complex has also used K-eTh-eU ternary relationships to assist the delineation of hydrothermal alteration zones [38]. Radiometric data have also been integrated with remote sensing at Wikki Warm Spring, northeastern Nigeria, to map spatial radiogenic patterns and assess geothermal potential [39]. The Maxwell colour triangle (Figure 4) showing the conceptual red-green-blue combination used in ternary radiometric displays.

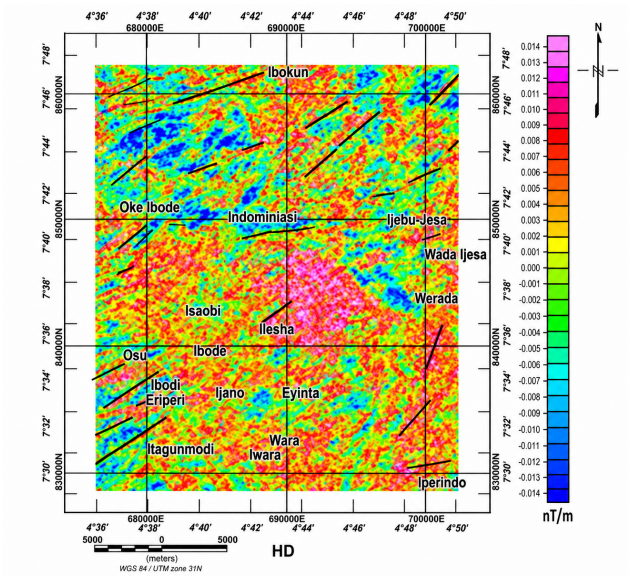

Figure 19: Horizontal derivative map showing prominent magnetic gradients interpreted as probable contacts and structural boundaries.

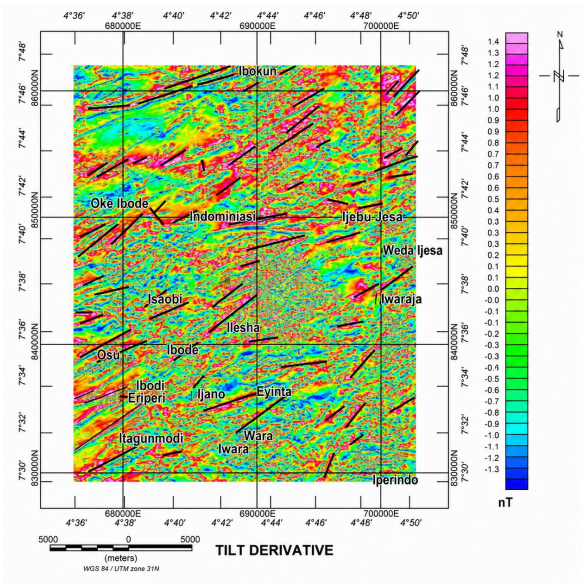

Figure 21: Tilt derivative map highlighting major magnetic edges and dominant structural trends.

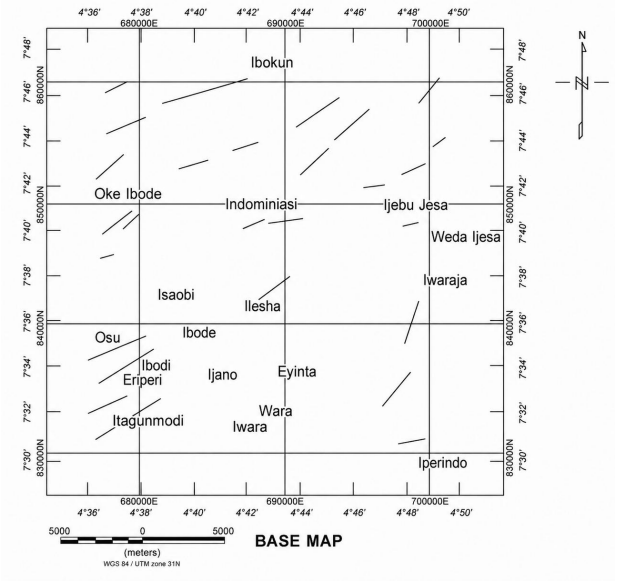

Figure 20: Lineaments interpreted from the horizontal derivative map.

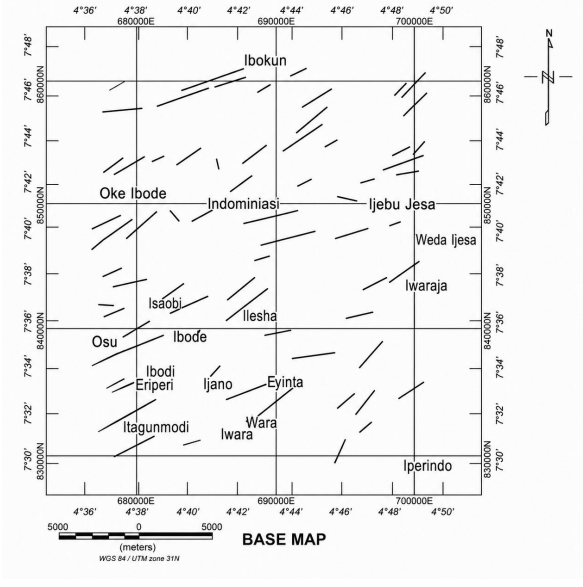

Figure 22: Lineaments interpreted from the tilt derivative map.

3.2. Aeromagnetic data processing and enhancement

The magnetic method responds to spatial variations in rock magnetisation and is widely used to map subsurface geological contacts and structures in mineral exploration [40–43]. Magnetic susceptibility (κ) relates induced magnetisation (M_i) to the applied magnetic field (H), such that M_i = κH, and is distinct from remanent magnetisation retained independently of the present field [4, 44, 45]. Because airborne magnetic anomalies may contain both induced and remanent components, particularly important at low magnetic latitude, the data were processed and enhanced to improve anomaly resolution and structural interpretation. The workflow comprised reduction to the equator (RTE), regional-residual separation, first derivatives, analytic-signal amplitude, tilt derivative, lineament interpretation and Euler deconvolution.

Magnetic highs and lows were interpreted primarily as relative magnetic responses, while lithological assignments were made only where supported by the geological framework. Structural lineaments were manually extracted from the analytic-signal, horizontal-derivative, tilt-derivative and first-vertical-derivative maps. Tracing was based on visually continuous or aligned linear to curvilinear magnetic gradients, anomaly breaks and source-edge responses that could represent subsurface structural boundaries. Only clearly defined and spa-

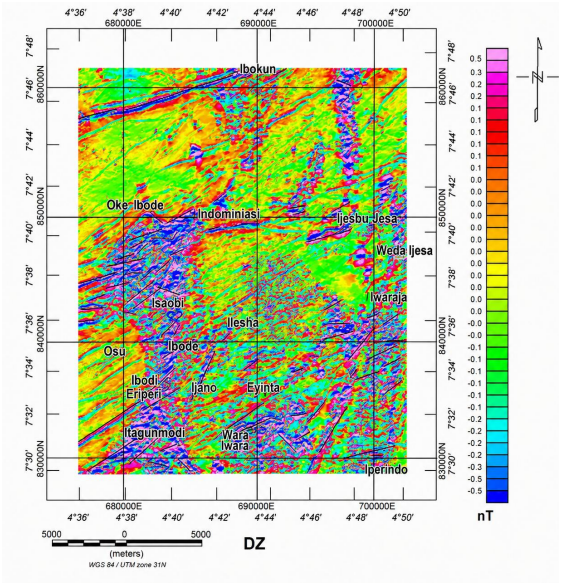

Figure 23: First vertical derivative map enhancing shallow magnetic anomalies, source boundaries, and linear structural features.

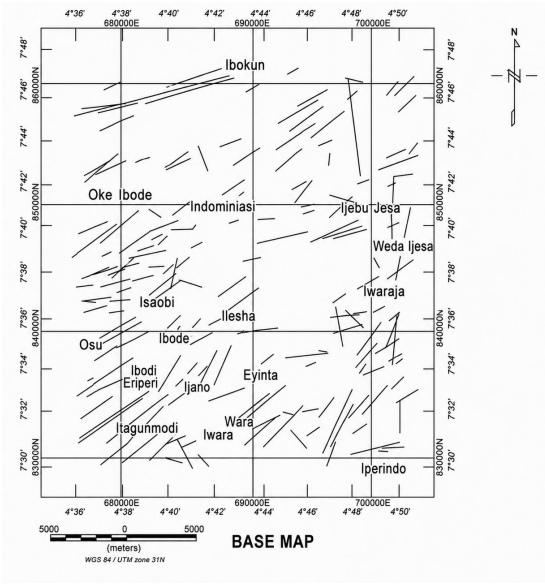

Figure 25: Composite lineament map showing the spatial distribution and dominant orientations of interpreted magnetic lineaments.

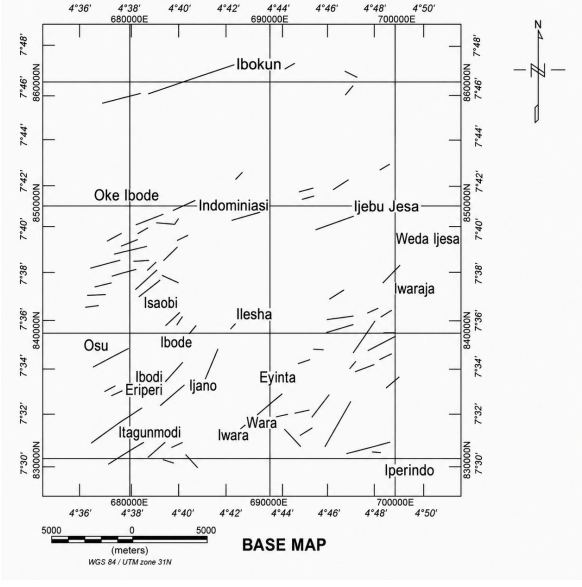

Figure 24: Structural lineaments from the first vertical derivative (FVD) aeromagnetic map.

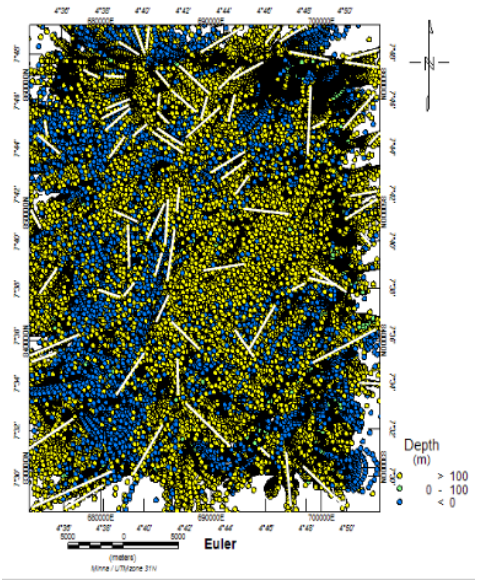

Figure 26: Euler deconvolution map showing clustered magnetic-source solutions and their estimated depth distribution.

tially coherent features were retained, while isolated, poorly defined or probable processing artefacts were excluded. The independently interpreted lineaments were subsequently combined to produce the composite lineament map.

The total magnetic anomaly represents the portion of the measured airborne magnetic field that remains after removal of the reference geomagnetic field [45].

$$\Delta T = T_{\text{observed}} - T_{\text{IGRF}}, \tag{1}$$

where ΔT = total magnetic anomaly, normally expressed in nT; Tobserved = magnetic field measured by the airborne magnetometer, in nT; TIGRF = geomagnetic reference field calculated from the International Geomagnetic Reference Field for the survey location, elevation, and observation epoch, in nT.

The horizontal gradient magnitude quantifies the lateral rate of change of the magnetic anomaly. Ridges or maxima in horizontal-gradient responses are commonly used to trace magnetisation boundaries and buried structural contacts [45, 48].

$$HD = \sqrt{\left(\frac{\partial T}{\partial x}\right)^2 + \left(\frac{\partial T}{\partial y}\right)^2}, \tag{2}$$

where HD = horizontal gradient magnitude of the magnetic field; T = magnetic anomaly field; x = east-west horizontal coordinate; y = north-south horizontal coordinate; $\partial T/\partial x$ = magnetic-field gradient in the x direction; $\partial T/\partial y$ = magnetic-field gradient in the y direction.

The first vertical derivative enhances short-wavelength magnetic components and sharpens anomaly boundaries. It is particularly useful for emphasizing relatively shallow magnetic sources and improving the visibility of contacts and lineaments, although it may also amplify high-frequency noise [45]

$$FVD = \frac{\partial T}{\partial z}, \tag{3}$$

where FVD = first vertical derivative of the magnetic anomaly; T = magnetic anomaly field; z = vertical coordinate, $\partial T/\partial z$ = rate of change of the magnetic field in the vertical direction.

The first-order x-derivative (Dx) was applied to measure the east-west rate of change of the magnetic anomaly field. The operator enhances lateral magnetic gradients and therefore improves the delineation of faults, joints, lithological contacts and other magnetic-source boundaries. The resulting derivative is expressed in nT/m.

$$D_x = \frac{\partial T}{\partial x}. \tag{4}$$

The second-order x-derivative (Dxx) was used to further sharpen short-wavelength magnetic variations and emphasize subtle lateral boundaries associated with shallow faults, contacts and closely spaced magnetic sources. Because second-order differentiation enhances high-frequency components, the result was interpreted together with the other magnetic derivative maps. The derivative is expressed in nT/m^2.

$$D_{xx} = \frac{\partial^2 T}{\partial x^2}, \tag{5}$$

where T is the magnetic anomaly field and x is the east-west spatial coordinate.

The three-dimensional analytic signal amplitude combines the two horizontal derivatives and the vertical derivative into a single positive quantity [27]. Peaks in the analytic signal commonly occur close to the edges of magnetized bodies, making the operator useful for delineating source boundaries where anomaly shape is complicated by the direction of magnetisation.

$$A(x,y) = \sqrt{\frac{\partial T^2}{\partial x} + \frac{\partial T^2}{\partial y} + \frac{\partial T^2}{\partial z}}, \tag{6}$$

where A(x, y) = analytic signal amplitude at map position (x, y); T = magnetic anomaly field; x = east-west coordinate; y = north-south coordinate; z = vertical coordinate; $\partial T/\partial x$, $\partial T/\partial y$, $\partial T/\partial z$ = magnetic gradients in the x, y, and z directions, respectively.

The tilt derivative normalizes the vertical derivative by the horizontal gradient magnitude [28]. This ratio compresses the large amplitude difference between shallow and deep sources, allowing weak and strong magnetic edges to be displayed on a comparable angular scale and aiding the tracing of structural contacts across the survey area.

$$TDR = \tan^{-1}\left[\frac{\frac{\partial T}{\partial z}}{\sqrt{\frac{\partial T^2}{\partial x} + \frac{\partial T^2}{\partial y}}}\right], \tag{7}$$

where TDR = tilt derivative or tilt angle, commonly expressed in radians or degrees; T = magnetic anomaly field; x = east-west coordinate; y = north-south coordinate; z = vertical coordinate; $\tan^{-1}$ = inverse tangent function.

According to Ref. [45], upward continuation predicts the magnetic field that would be observed at a greater elevation above the sources. In the frequency domain it suppresses short-wavelength components more strongly than long-wavelength components, thereby attenuating shallow-source effects and emphasizing broader anomalies associated with deeper regional sources.

$$F(k_x, k_y, z) = F(k_x, k_y, 0)\, e^{-kz}, \tag{8}$$

$$k = \sqrt{k_x^2 + k_y^2}, \tag{9}$$

where $F(k_x, k_y, 0)$ = Fourier transform of the magnetic field at the original survey level; F(kx,ky,z) = Fourier transform of the upward-continued field at continuation height z; kx = wavenumber in the x direction; ky = wavenumber in the y direction; k = total radial wavenumber, $\sqrt{k_x^2 + k_y^2}$; z = upward continuation distance; e = base of the natural logarithm. The exponential factor e^{-kz} acts as a low-pass filter. Consequently, progressively larger continuation heights produce smoother fields and reduce the contribution of shallow magnetic sources.

Euler deconvolution estimates the location and depth of magnetic sources by applying Euler's homogeneity relation to the anomaly field and its spatial derivatives [31]. The method is useful for identifying clusters of depth solutions associated with contacts, dykes, pipes, and compact magnetic bodies, provided that an appropriate structural index and solution-selection criteria are used. Comparable aeromagnetic studies have combined Euler deconvolution with derivative and edge-based methods to map basement depths and contact locations [49].

$$\begin{aligned}(x - x_0)\frac{\partial T}{\partial x} + (y - y_0)\frac{\partial T}{\partial y} \\ + (z - z_0)\frac{\partial T}{\partial z} = N(B - T)\end{aligned}, \tag{10}$$

where (x, y,z) = coordinates of the observation point; (x_0,y_0,z_0) = coordinates of the estimated source position; T = observed magnetic anomaly; B = regional or background magnetic-field level within the solution window; $\partial T/\partial x$, $\partial T/\partial y$, $\partial T/\partial z$ = spatial derivatives of the magnetic anomaly; N = structural index, which describes the rate at which the field decreases with distance from an idealized source.

For the conventional magnetic-field formulation, commonly used structural indices are N = 0 for a contact or step, N = 1 for

a dyke or sill, N = 2 for a cylindrical or pipe-like source, and N = 3 for a sphere or compact three-dimensional body. The values should be selected to reflect the expected source geometry and tested for geological consistency.

Aeroradiometric processing was used to examine the relative distribution of the principal naturally occurring radioelements represented by potassium (K), equivalent uranium (eU), and equivalent thorium (eTh). Ratio and composite parameters are useful for highlighting relative enrichment or depletion patterns.

The K/eTh ratio compares the relative abundance of potassium with thorium [23].

$$R_{K/eTh} = \frac{K}{eTh}, \tag{11}$$

where K = potassium concentration, commonly reported as % K, eTh = equivalent thorium concentration, commonly reported as ppm eTh; R_K/Th = potassium-to-thorium ratio.

The F-parameter combines potassium and uranium relative to thorium and is commonly used as a composite radiometric index of relative K-U enrichment [50]. It can assist in screening areas where more than one radiometric criterion is elevated, but anomalous values require comparison with the individual radioelement channels and mapped geology.

$$F = \frac{K \times U}{Th}, \tag{12}$$

where F = F-parameter or composite radiometric ratio; K = potassium concentration, commonly expressed as % K; U = equivalent uranium concentration, commonly expressed as ppm eU; Th = equivalent thorium concentration, commonly expressed as ppm eTh.

4. Results and discussion

The potassium map (Figure 5) shows the distribution of potassium concentration across the study area. Blue–green colours (0.2–0.4%) indicate areas with low potassium concentration. High potassium concentrations (red–pink) around 0.6–2.4% indicate potassium-rich rocks such as granites and feldspar-rich lithologies and may also suggest zones of potassic hydrothermal alteration associated with mineralisation.

The thorium map (Figure 6) illustrates the variation in thorium concentration within the study area. Blue–green colours (5.4–10.7 ppm) represent low thorium concentrations, while red–pink colours (13–23.8 ppm) indicate high thorium concentrations. High thorium values generally reflect felsic intrusive rocks and resistant minerals such as monazite and zircon, whereas low values may indicate mafic rocks or weathered terrains.

The uranium map (Figure 7) shows the distribution of uranium concentration. Blue–green colours (0.6–2.3 ppm) represent low uranium concentrations, while red–pink colours (2.5–4.9 ppm) indicate high uranium concentrations. Areas with elevated uranium values may indicate zones of hydrothermal alteration, joints or uranium enrichment, whereas low values represent areas with minimal uranium content.

The K/eTh ratio map (Figure 8) shows relative potassium enrichment with respect to thorium across the study area. Low K/eTh values, represented mainly by blue-green colours and approaching 0, indicate relatively low K/eTh responses that may reflect Th enrichment, K depletion, lithological variation or near-surface weathering effects. Higher K/eTh values, shown by red-pink colours and concentrated mainly in the northern and southern parts of the area, indicate relative K enrichment or Th depletion. These responses are not uniquely diagnostic of hydrothermal alteration but may be considered potential alteration indicators only where they coincide with favourable geological and structural features. The F-parameter map (Figure 9) ranges from approximately 0 to 0.5. Blue-green colours, generally around 0–0.1, represent low relative K-eU enrichment with respect to eTh, whereas red-pink colours, approximately 0.1–0.5, occur prominently in the northern and southeastern sectors and define comparatively stronger radiometric anomalies.

These elevated F-parameter responses are prospective radiometric indicators rather than direct evidence of hydrothermal mineralisation. However, elevated F-parameter responses gain greater significance where they correspond spatially with magnetic lineaments, structural intersections and lithological contacts. The ternary K-eTh-eU composite map (Figure 10) further illustrates spatial variations in the relative abundance of the three radioelements, with red, green and blue representing relative enrichment in K, eTh and eU, respectively. Whitish tones in parts of the northern and southeastern sectors represent relatively high combined responses of the three radioelements, whereas darker tones indicate comparatively low total radiometric response. These colour patterns may reflect lithological composition, weathering or alteration.

The TMI map (Figure 11) represents the total magnetic field of the study area. Blue–green colours (-208.3 to -6.4 nT) correspond to low magnetic intensity, which may be associated with hydrothermally altered rock or thick sediment cover while red–pink colours (46.1–149.7 nT) represent high magnetic intensity, indicating ultramafic rocks and iron formation.

The RTE map (Figure 12) corrects magnetic anomalies due to the study area's low magnetic latitude. Blue–green colours (-188.4 to -0.5 nT) indicate low magnetic TMI, whereas red–pink colours (58–123.3 nT) indicate high magnetic TMI. The correction improves the positioning of magnetic anomalies directly over their causative sources, making geological structures easier to interpret. The RTE magnetic field was upward continued to a height of 2,000 m to suppress short-wavelength anomalies associated with shallow magnetic sources and emphasize the broader regional magnetic field. The resulting upward-continued field constitutes the regional magnetic map presented in Figure 13. The regional map (Figure 13) suppresses shallow anomalies and enhances deeper magnetic features. Blue–green colours (-173–1.2 nT) represent weak magnetic contrasts, while red–pink colours (47.2–123.6 nT) indicate strong magnetic contrast. In the northern part of the map, the pattern reveals the regional structural framework and major geological structures controlling hydrothermal fluids.

The residual map (Figure 14) shows the local, shallow magnetic component (high-frequency component) after removal

of the regional field. Blue–green colours (-96.5 to -0.4 nT) represent weak magnetic contrasts, while red–pink colours (22.4–75.6 nT) indicate strong magnetic contrast. The residual magnetic pattern reveals several localized positive and negative anomalies that are interpreted primarily as shallow magnetic sources rather than direct indicators of mineralisation. In this study, priority prospective zones were defined where residual magnetic anomalies spatially coincide with mapped magnetic contacts or lineaments and anomalous radiometric responses, particularly elevated K/eTh and F-parameter values. The analytic signal map (Figure 15) enhances the edges of magnetic sources irrespective of magnetisation direction. Low analytic signal amplitudes (blue–green) around (0–01nT) represent weak magnetic contrasts, while high amplitudes (red–pink) around (0.3–1.2nT) indicate strong magnetic contacts that may be faults, lithological boundaries and possible mineralized structures.

The lineament map (Figure 16), extracted from the analytic signal highlights structural features such as faults, joints and contacts. Areas with dense lineaments represent zones of structural complexity and are favourable pathways for hydrothermal fluids and mineral deposition. The first-order derivative in the X-direction (Figure 17) enhances magnetic gradients along the east-west direction. High-gradient zones indicate the sudden change in magnetic susceptibility that is caused by lithological contacts, faults, or dykes. The second-order derivative in the x-direction (Figure 18) enhances magnetic anomalies. It enhances subtle structural features and improves the delineation of shallow faults, contacts, and joint zones. The horizontal derivative map (Figure 19) enhances shallow geological contacts and structural boundaries. Blue–green colours indicate areas with weak magnetic gradients, while red–pink colours indicate strong gradients corresponding to lithological contacts, faults and joints. Figure 20 presents the lineaments interpreted from the horizontal derivative map. The mapped lineaments define major structural trends that may control fluid migration and mineralisation. The tilt derivative map (Figure 21) enhances both weak and strong magnetic anomalies equally. Blue–green colours (-.1.3–0.2 radians) indicate relatively weak magnetic responses, whereas red–pink (0.8–1.4 radians) colours represent strong magnetic contrasts associated with structural boundaries and lithological contacts.

Figure 22 displays the structural lineaments extracted from the tilt derivative map. The mapped structures reveal the orientation and continuity of faults and joints that may influence mineralisation. The first vertical derivative map (Figure 23) emphasizes shallow magnetic sources and suppresses deeper regional anomalies. Blue–green colours (-0.5–0 nT/m) indicate relatively weak magnetic responses, whereas red–pink colours (0.1–0.5 nT/m) indicate strong shallow magnetic anomalies related to near-surface structures, contacts and intrusive bodies. Figure 24 presents the lineaments interpreted from the first vertical derivative map. The extracted structures represent faults, joints, and contacts that may serve as channels for hydrothermal fluid movement and mineral deposition.

The composite lineament map (Figure 25) represents the spatial distribution and density of structural features interpreted from the derivative and edge-enhancement products. Zones with closely spaced and intersecting mapped lineaments are interpreted as areas of greater structural complexity associated with faults, joints, and lithological contacts. Such zones are important to the integrated interpretation because they may provide favourable structural pathways. The Euler deconvolution map (Figure 26) defines the distribution and depth of magnetic sources in the study area. The yellow solutions represent deeper magnetic sources, and their widespread occurrence does not imply that the entire study area is mineralised. Prospectivity is mainly associated with zones where Euler solution clusters coincide with magnetic lineaments, structural intersections and sharp magnetic gradients, indicating control by faults, joints and lithological contacts that may have acted as hydrothermal fluid pathways. The result indicates localized structurally controlled prospective zones rather than uniform mineralisation across the study area.

5. Conclusion

The integrated interpretation of aeromagnetic and airborne gamma-ray spectrometric data has provided a coherent framework for delineating structurally and radiometrically prospective zones within part of the Ife-Ilesha Schist Belt. The radiometric datasets show potassium concentrations of approximately 0.2–2.4%, equivalent thorium values of 5.4–23.8 ppm, and equivalent uranium concentrations of 0.6–4.9 ppm, while the total magnetic intensity, reduction-to-equator, and residual magnetic fields range from about -208.3 to 149.7 nT, -188.4 to 123.3 nT, and -96.5 to 75.6 nT, respectively. The integrated analysis successfully delineates lithological variations, magnetic contacts, structural lineaments, and zones of contrasting radioelement distribution across the study area. Rather than treating isolated magnetic or radiometric anomalies as direct evidence of hydrothermal mineralisation, the interpretation identifies prospective zones on the basis of spatial coincidence between independent geophysical criteria. Structurally favourable magnetic edges and lineaments associated with relative potassium enrichment, elevated K/eTh ratios, and enhanced F-parameter responses provide the principal basis for recognizing areas that may have experienced structurally controlled hydrothermal alteration.

The most prominent priority targets occur mainly within the northern and southeastern sectors of the study area, where magnetic structural features coincide with favourable radiometric signatures. These coincidence anomalies are considered more geologically significant than single-dataset responses and therefore represent the most prospective zones for follow-up investigation. The study demonstrates the value of integrating aeromagnetic and Aeroradiometric datasets for regional structural mapping and first-pass mineral prospectivity assessment in the Ife-Ilesha Schist Belt, while emphasizing the need for subsequent geological mapping, geochemical sampling, and ground geophysical surveys to validate the identified targets.

Data availability

The aeromagnetic and aeroradiometric datasets supporting the findings of this study were obtained from the Nigerian Geological Survey Agency (NGSA) and are available from the Agency upon request.

Declaration of competing interest

The authors declare that they have no known competing financial interests or personal relationships that could have appeared to influence the work reported in this manuscript.

Funding

The authors received no specific funding from any public, commercial, or not-for-profit organisation for this research.

Acknowledgment

The authors acknowledge the Nigerian Geological Survey Agency (NGSA) for providing access to the airborne magnetic and gamma-ray spectrometric datasets used in this study.

References

[1] F. Pirajno, *Hydrothermal processes and mineral systems*, Springer, Dordrecht, Netherlands, 2009 https://doi.org/10.1007/978-1-4020-8613-7.

[2] L. J. Robb, *Introduction to ore-forming processes*, Blackwell Publishing, Oxford, United Kingdom, 2005. https://openlibrary.org/books/OL17126435M/Introduction_to_ore-forming_processes.

[3] L. S. Adebiyi, A. B. Eluwole, A. O. Fajana, N. B. Salawu, S. C. Falade, K. O. Dopamu & E. A. Alejolowo, "Integrated geophysical methods for delineating crustal structures and hydrothermal alteration zones for mineral exploration projects in parts of west-central Nigeria", Modeling Earth Systems and Environment **8** (2022) 2977 https://doi.org/10.1007/s40808-021-01275-5.

[4] P. Kearey, M. Brooks & I. Hill, *An introduction to geophysical exploration*, 3rd ed., Wiley-Blackwell, Chichester, United Kingdom, 2002. https://www.wiley-vch.de/en/areas-interest/natural-sciences/earth-science-11es/geology-geophysics-11es1/geophysics-11es12/an-introduction-to-geophysical-exploration-978-0-632-04929-5.

[5] International Atomic Energy Agency, "Guidelines for radioelement mapping using gamma ray spectrometry data", IAEA-TECDOC-1363, Vienna, Austria, 2003 https://www.iaea.org/publications/6746.

[6] S. O. Elkhateeb & M. A. G. Abdellatif, "Delineation potential gold mineralisation zones in a part of Central Eastern Desert, Egypt using airborne magnetic and radiometric data", NRIAG Journal of Astronomy and Geophysics **7** (2018) 361 https://doi.org/10.1016/j.nrjag.2018.05.010.

[7] R. B. K. Shives, B. W. Charbonneau & K. L. Ford, "The detection of potassic alteration by gamma-ray spectrometry-recognition of alteration related to mineralisation", Geophysics **65** (2000) 2001 https://doi.org/10.1190/1.1444884.

[8] N. G. Obaje, *Geology and mineral resources of Nigeria*, Springer, Berlin, Germany, 2009 https://doi.org/10.1007/978-3-540-92685-6.

[9] A. A. Elueze, "Petrology and gold mineralization of the amphibolite belt, Ilesha area, Southwestern Nigeria", Geologie en Mijnbouw **65** (1986) 189 https://njgjournal.nl/index.php/njg/article/view/13141.

[10] R. Caby & J.-M. Boessé, "Pan-African nappe system in southwest Nigeria: the Ife-Ilesha schist belt", Journal of African Earth Sciences **33** (2001) 211 https://doi.org/10.1016/S0899-5362(01)80060-9.

[11] K. O. Olomo, S. Bayode, O. A. Alagbe, G. M. Olayanju & O. K. Olaleye, "Aeromagnetic mapping and radioelement influence on mineralogical composition of mesothermal gold deposit in part of the Ilesha Schist Belt, southwestern Nigeria", NRIAG Journal of Astronomy and Geophysics **11** (2022) 177 https://doi.org/10.1080/20909977.2022.2057147.

[12] A. A. Akinlalu, G. M. Olayanju, K. A. N. Adiat & G. O. Omosuyi, "Mineralisation potential assessment using analytical hierarchy process modelling technique: a case study of Ilesha Schist Belt, southwestern Nigeria", Results in Geophysical Sciences **7** (2021) 100026 https://doi.org/10.1016/j.ringps.2021.100026.

[13] J. S. Kayode, M. N. M. Nawawi, K. Abdullah & A. E. Khalil, "Integrating aeromagnetic and Landsat 8 data into subsurface structural mapping of Precambrian Basement Complex", Journal of African Earth Sciences **125** (2017) 202 https://doi.org/10.1016/j.jafrearsci.2016.11.010.

[14] O. S. Ogungbemi, J. O. Amigun & G. M. Olayanju, "Geophysical characterization of mineralization potential of eastern parts of Ife-Ijesha Schist Belt, southwestern Nigeria", International Journal of Scientific & Technology Research **7** (2018) 21. https://www.researchgate.net/publication/330686720_Geophysical_characterization_of_mineralization_potential_of_eastern_parts_of_Ife-Ijesha_Schist-Belt_southwestern_Nigeria.

[15] A. A. Akinlalu, "Radiometric mapping for the identification of hydrothermally altered zones related to gold mineralisation in Ife Ilesa Schist Belt, Southwestern Nigeria", Indonesian Journal of Earth Sciences **3** (2023) A519 https://doi.org/10.52562/injoes.2023.519.

[16] A. A. Akinlalu, A. O. Adelusi, G. M. Olayanju, K. A. N. Adiat, G. O. Omosuyi, A. Y. B. Anifowose & B. E. Akeredolu, "Aeromagnetic mapping of basement structures and mineralisation characterisation of Ilesa Schist Belt, Southwestern Nigeria", Journal of African Earth Sciences **138** (2018) 383 https://doi.org/10.1016/j.jafrearsci.2017.11.033.

[17] N. B. Salawu, J. O. Fatoba, L. S. Adebiyi, M. M. Orosun & S. S. Dada, "New insights on the Ife-Ilesha schist belt using integrated satellite, aeromagnetic and radiometric data", Scientific Reports **11** (2021) 15314 https://doi.org/10.1038/s41598-021-94813-1.

[18] I. C. Okeyode, O. T. Olurin, S. A. Ganiyu & J. A. Olowofela, "High resolution airborne radiometric and magnetic studies of Ilesha and its environs, southwestern Nigeria", Materials and Geoenvironment **66** (2019) 51 https://doi.org/10.2478/rmzmag-2018-0020.

[19] A. M. Eldosouky, M. Abdelkareem & S. O. Elkhateeb, "Integration of remote sensing and aeromagnetic data for mapping structural features and hydrothermal alteration zones in Wadi Allaqi area, South Eastern Desert of Egypt", Journal of African Earth Sciences **130** (2017) 28 https://doi.org/10.1016/j.jafrearsci.2017.03.006.

[20] L. S. Adebiyi, A. B. Eluwole, A. O. Fajana & N. B. Salawu, "A preliminary geophysical investigation of lead mineralisation in parts of the crystalline basement complex of Nigeria", Modeling Earth Systems and Environment **10** (2024) 371 https://doi.org/10.1007/s40808-023-01782-7.

[21] K. Ford, J. R. Harris, R. Shives, J. Carson & J. Buckle, " Remote predictive mapping 2. Gamma-ray spectrometry: a tool for mapping Canada's North", Geoscience Canada **35** (2008) 109 https://journals.lib.unb.ca/index.php/gc/article/view/11270.

[22] B. R. S. Minty, "Fundamentals of airborne gamma-ray spectrometry", AGSO Journal of Australian Geology and Geophysics **17** (1997) 39. https://www.researchgate.net/publication/279937934_Fundamentals_of_airborne_gamma-ray_spectrometry

[23] B. L. Dickson & K. M. Scott, "Interpretation of aerial gamma-ray surveys-adding the geochemical factors", AGSO Journal of Australian Geology and Geophysics **17** (1997) 187. https://www.researchgate.net/publication/265644072_Interpretation_of_aerial_gamma-ray_surveys_-_adding_the_geochemical_factors

[24] L. S. Adebiyi, A. B. Eluwole, A. O. Fajana, N. B. Salawu, S. C. Falade, K. O. Dopamu & E. A. Alejolowo, "Analysis of airborne magnetic and gamma-ray spectrometry data for the geothermal source and conduits of the Ikogosi warm spring, southwestern Nigeria", Arabian Journal of Geosciences **15** (2022) 630 https://doi.org/10.1007/s12517-022-09874-x.

[25] M. Dentith, H. Yuan, S. Johnson, R. Murdie & P. Piña-Varas, "Application of deep-penetrating geophysical methods to mineral exploration: examples from Western Australia", Geophysics **83** (2018) WC29 https://doi.org/10.1190/geo2017-0482.1.

[26] J. D. Phillips, "Locating magnetic contacts: a comparison of the horizontal gradient, analytic signal, and local wavenumber methods", SEG Technical Program Expanded Abstracts **2000** (2000) 402 https://doi.org/

10.1190/1.1816078.
[27] M. N. Nabighian, "The analytic signal of two-dimensional magnetic bodies with polygonal cross-section: its properties and use for automated anomaly interpretation", Geophysics **37** (1972) 507 https://doi.org/10.1190/1.1440276.
[28] H. G. Miller & V. Singh, "Potential field tilt-a new concept for location of potential field sources", Journal of Applied Geophysics **32** (1994) 213 https://doi.org/10.1016/0926-9851(94)90022-1.
[29] W. R. Roest, J. Verhoef & M. Pilkington, "Magnetic interpretation using the 3-D analytic signal", Geophysics **57** (1992) 116 https://doi.org/10.1190/1.1443174.
[30] A. B. Reid, J. M. Allsop, H. Granser, A. J. Millett & I. W. Somerton, "Magnetic interpretation in three dimensions using Euler deconvolution", Geophysics **55** (1990) 80 https://doi.org/10.1190/1.1442774.
[31] D. T. Thompson, "EULDPH: a new technique for making computer-assisted depth estimates from magnetic data", Geophysics **47** (1982) 31 https://doi.org/10.1190/1.1441278.
[32] S. M. Gandhi & B. C. Sarkar, *Essentials of mineral exploration and evaluation*, Elsevier, Amsterdam, Netherlands, 2016 https://doi.org/10.1016/C2015-0-04648-2.
[33] M. A. Rahaman, "Recent advances in the study of the Basement Complex of Nigeria", in *Precambrian Geology of Nigeria*, Geological Survey of Nigeria, Kaduna, Nigeria, 1988, pp. 11–43.
[34] A. C. Ajibade, M. Woakes & M. A. Rahaman, "Proterozoic crustal development in the Pan-African regime of Nigeria", in *Proterozoic Lithospheric Evolution*, A. Kröner (Ed.), Geodynamics Series, vol. 17, American Geophysical Union, 1987, pp. 259–271. https://doi.org/10.1029/GD017p0259.
[35] R. W. J. Keay, *An outline of Nigerian vegetation*, Government Printer, Lagos, Nigeria, 1959. https://search.worldcat.org/title/An-outline-of-Nigerian-vegetation/oclc/17224424.
[36] P. O. Oluyide, "Structural trends in the Nigerian Basement Complex", in *Precambrian Geology of Nigeria*, Geological Survey of Nigeria, Kaduna, Nigeria, 1988, pp. 93–98.
[37] I. B. Odeyemi, "A comparative study of remote sensing images of the structure of the Okemesi Fold Belt, Nigeria", ITC Journal **1** (1993) 77.
[38] J. A. Bwamba, A. Mallam & A. U. Osagie, "Characterization of hydrothermal alteration zones in parts of north-central Basement Complex of Nigeria for solid mineral deposits", Earth Sciences Pakistan **8** (2024) 126 https://doi.org/10.26480/esp.02.2024.126.133.
[39] N. B. Salawu, A. B. Eluwole, A. O. Fajana, M. M. Orosun, L. S. Adebiyi & J. O. Salawu, "New perspective on the geothermal potential of Wikki Warm Spring, Northeastern Nigeria, from remote sensing and radiometric data", Acta Geophysica **72** (2024) 1867 https://doi.org/10.1007/s11600-023-01098-1.
[40] M. C. Dentith & S. T. Mudge, *Geophysics for the mineral exploration geoscientist*, Cambridge University Press, Cambridge, United Kingdom, 2014 https://doi.org/10.1017/CBO9781139024358.
[41] L. S. Adebiyi, A. B. Eluwole, A. O. Fajana, N. B. Salawu & A. Saleh, "Contrasting structures of the Southern Benue trough and the contiguous crystalline basement as observed from high-resolution aeromagnetic data", Scientific Reports **13** (2023) 21516 https://doi.org/10.1038/s41598-023-48639-8.
[42] A. O. Fajana, J. Amosun, H. Abiodun, J. Tsado & A. Owasanoye, "Aeromagnetic and remote sensing application for groundwater exploration in Oye and its environs", Journal of Innovation Science and Technology **2** (2022) 1 https://jist.fuoye.edu.ng/index.php/jist/article/view/25.
[43] A. O. Fajana, "Assessment of the reliability of magnetic method to delineate geologic features in a Basement Complex: a case study of Phase 1, Federal University Oye", Journal of Scientific and Engineering Research **3** (2016) 1 https://jsaer.com/download/vol-3-iss-2-2016/JSAER2016-03-02-1-7.pdf.
[44] W. M. Telford, L. P. Geldart & R. E. Sheriff, *Applied geophysics*, 2nd ed., Cambridge University Press, Cambridge, United Kingdom, 1990 https://doi.org/10.1017/CBO9781139167932.
[45] R. J. Blakely, *Potential theory in gravity and magnetic applications*, Cambridge University Press, Cambridge, United Kingdom, 1995 https://doi.org/10.1017/CBO9780511549816.
[46] H. Li, Q. Zhang, M. Pan, D. Chen, Z. Liu, L. Yan, Y. Xu, Z. Ding, Z. Yu, X. Liu, K. Wan & W. Dai, "Accounting for geometric anisotropy in sparse magnetic data using a modified interpolation algorithm", Remote Sensing **16** (2024) 883 https://doi.org/10.3390/rs16050883.
[47] J. C. Maxwell, "On the theory of compound colours, and the relations of the colours of the spectrum", Philosophical Transactions of the Royal Society of London **150** (1860) 57 https://doi.org/10.1098/rstl.1860.0005.
[48] L. Cordell & V. J. S. Grauch, "Mapping basement magnetisation zones from aeromagnetic data in the San Juan Basin, New Mexico", in *The Utility of Regional Gravity and Magnetic Anomaly Maps*, W. J. Hinze (Ed.), Society of Exploration Geophysicists, 1985, pp. 181–197 https://doi.org/10.1190/1.0931830346.ch16.
[49] M. A. Al-Badani & Y. M. Al-Wathaf, "Using the aeromagnetic data for mapping the basement depth and contact locations at southern part of Tihamah region, western Yemen", Egyptian Journal of Petroleum **27** (2018) 485 https://doi.org/10.1016/j.ejpe.2017.07.015.
[50] I. S. Sobolev, A. N. Orekhov & N. P. Soboleva, "Use of multivariate statistics elements for ground gamma-ray spectrometry data processing in exploration of hydrothermal gold deposits", Bulletin of the Tomsk Polytechnic University, Geo Assets Engineering **329** (2018) 104. https://izvestiya.tpu.ru/archive/article/view/2064.